

# Stochastic Aspects of Mass Transport in Gas Diffusion Layers

Dieter Froning<sup>1</sup>, Gerd Gaiselmann<sup>2</sup>, Uwe Reimer<sup>1</sup>, Jan Brinkmann<sup>1</sup>, Volker Schmidt<sup>2</sup>, Werner Lehnert<sup>1,3</sup>

<sup>1</sup>Forschungszentrum Jülich GmbH, Institute of Energy and Climate Research, IEK-3: Electrochemical Process Engineering

<sup>2</sup>Institute of Stochastics, Ulm University

<sup>3</sup>Modeling in Electrochemical Process Engineering, RWTH Aachen University

## Abstract

The relationship between the 3D morphology of gas-diffusion layers (GDL) of HT-PEFCs and their functionality is analyzed. A stochastic model describing the microstructure of paper-type GDL is combined with the Lattice-Boltzmann method (LBM) to simulate gas transport within the GDL microstructure. Virtual 3D microstructures representing paper-type GDL are generated by a stochastic model, where the binder morphology is systematically modified. On these structures single phase, single component gas flow is computed by the LBM. Quality criteria evaluating the spatial homogeneity of gas supply are introduced and related to the binder morphology. The spatial homogeneity of the gas supply is analyzed by a parametrized stochastic model describing the gas flow at the exit of the GDL. This approach gives insight into the spatial structure of the gas flow at the GDL exit. The quality of gas supply is quantified by characterizing size and arrangement of regions with high gas supply. This stochastic gas flow model predicts the quality of gas supply for further binder morphologies. Analyzing the quality criteria and the stochastic evaluation of the spatial structure of the gas flow field at the GDL exit, it is found that the binder morphology has an essential influence on the gas supply.

## Keywords

*paper-type GDL, stochastic modeling, microstructure, Lattice-Boltzmann, virtual materials design, mass transport, gas supply*

# 1 Introduction

Polymer electrolyte fuel cells (PEFC) are an attractive instrument for electrical power generation due to their high efficiency and environment-friendly emissions. A typical PEFC consists of several parts, namely the flow fields, gas-diffusion layers (GDL) and membrane electrode assembly<sup>1</sup>. At the membrane electrode assembly the electrochemical reactions take place. The flow fields provide the reacting gases and remove liquid and gaseous products. The function of the GDL is to provide a homogeneous mass transport between the flow field, where the typical size of a channel cross section is 1 mm, and the membrane electrode assembly. In case of high temperature PEFC (HT-PEFC) with a working temperature above 100 °C mass transport takes place in the gas phase solely. In addition, the GDL have to provide electrical contact between the flow field and the electrode layer. Different materials are used for GDL: carbon paper, carbon cloth and non-woven with typical fiber diameters of 5-10  $\mu\text{m}$  and a total thickness of the GDL between 100-300  $\mu\text{m}$ <sup>2;3</sup>. It is well-known that the 3D microstructure of the GDL has a large influence on the functionality and efficiency of PEFC<sup>4-8</sup>. Thus, the detection of ‘optimal’ microstructures is an important yet challenging task. In the industrial practice, however, the GDL is optimized by means of cost- and time-consuming experiments mainly based on a trial-and-error basis. Thus, a more systematic way to optimize GDL structures with respect to their functionality (e.g. gas supply of electrodes), is desirable. One possibility in this context is to perform *virtual materials design*, where a large variety of (e.g. synthetic, but) realistic GDL structures is generated in a systematic manner and their functionality is evaluated by numerical mass transport simulations. In this way, it is possible to detect microstructures with improved properties by means of (cost- and time-efficient) computer experiments.

To generate a large variety of realistic GDL structures, stochastic (parametrized) microstructure models can be used which provide 3D images describing the 3D microstructure of GDL. In contrast to the generation of experimental 3D image data, the advantage of using a stochastic microstructure model is that a large quantity of realistic material samples of GDL can be generated with arbitrarily large domain sizes, with low costs and in short time. Furthermore, the values of the model parameters can be varied such that important structural features (as e.g. porosity or binder morphology) of GDL are modified in a systematic manner.

Regarding the simulation of mass flow in the GDL, there are two general

approaches. The geometry of the GDL can either be treated as pseudo-homogeneous and some morphological features can be incorporated into continuum models<sup>9-13</sup>, or the entire geometry information can be used to simulate mass flow<sup>8;14-26</sup>. Note that the commonly applied methods in numerical transport simulation that consider the entire geometry information are the *computational fluid dynamics (CFD)* and the *Lattice-Boltzmann (LB)* algorithm. Also note that the pseudo-homogeneous approach (continuum models) without resolution of the inner structure of GDL is of advantage if the focus is on overall functionality of the fuel cells. In the present paper, however, we aim to obtain detailed information on the relation between morphological features of GDL and their functionality. Thus, the numerical transport simulations (which consider the entire structural information of GDL) are the right choice. In particular, we use the LB algorithm.

In this paper, we study the relationship between the 3D morphology of GDL in PEFC and their functionality. In particular, we investigate the influence of the binder morphology in paper-type GDL on the gas supply of electrodes which is one of the main tasks of GDL. The principal idea is to generate virtual (but realistic) 3D microstructures representing paper-type GDL using a stochastic simulation model, where the binder morphology is modified in a systematic manner. On these structures single phase, single component gas flow is computed by the LB method. Subsequently, the gas flow simulations are analyzed, evaluated and correlated with the corresponding binder morphologies. As reference system for the mass transport, we chose the case of mass transport at the anode side of a HT-PEFC, where the only fluid is gaseous hydrogen. Moreover, we focus on the structure of Toray 090 GDL belonging to the class of paper-type GDL. Note that paper-type GDL have a complex microstructure consisting of straight fibers and a binder which agglutinates the fibers.

In literature, there exist many stochastic simulation models describing the microstructure of paper-type GDL, see e.g.<sup>25;27-30</sup>. In the present paper, we use the multi-layer model proposed in<sup>29</sup> to generate virtual GDL consisting of a system of straight fibers and binder. This model is characterized by very few parameters and it offers the possibility to easily modify the binder morphology. Note that the model proposed in<sup>29</sup> has been successfully validated against experimental 3D image data of Toray 090 GDL.

To investigate the influence of binder in Toray 090 GDL on their functionality, we generate virtual Toray 090 GDL microstructures with different binder morphologies according to our stochastic model. Altogether, we compare

five different types of binder morphologies, ranging from a homogeneously spread binder (i.e., many areas of binder with small volumes) to a clustered binder (i.e., small number of areas with binder having large volumes). For all simulations, the total binder volume is kept constant. To enhance the statistical accuracy of the results, for each type of binder morphology, 25 independent samples of 3D microstructures are drawn from the stochastic GDL model. On these virtual GDL, gas flow is simulated via the LB method. The major goal of our investigations is the analysis and characterization of the gas flow and its local inhomogeneities related to the microstructure of the GDL. Subsequently, a new approach for analyzing and evaluating the fields of gas flow is considered and the obtained results are correlated to the corresponding binder morphology. For a conceptual overview on this analysis, see Figure 1.

To begin with, we introduce *quality criteria* to quantify the goodness of the mass flow computed by the LB method with respect to *spatial homogeneity*. Recall that the task of the GDL is to serve the electrodes with gas flux. In order to increase the conversion at the electrodes (and thus the power generation of the fuel cell), the gas flow field at the exit of the GDL should be as homogeneous as possible. However, it is not straight-forward how to compare two gas flow fields with respect to their spatial homogeneity, i.e., to decide which field is ‘more homogeneous’. Thus, we introduce quality criteria which quantify the *spatial homogeneity* of the gas flow field at the exit of the GDL. These quality criteria are based on statistical characteristics and are computed for all gas flow simulations. It is found that large clusters of binder material are unfavorable for a homogeneous gas flux.

Moreover, the statistical significance of mass transport simulations in typical domain sizes of experimental (tomographic) 3D image data is studied. It is found that the quality of the gas flux simulations exhibit large variations dependent on the concrete realization of the microstructure. Consequently, to accurately measure effects of mass transport related to 3D microstructures, it is necessary to average over several independently sampled microstructures.

In a further step, the gas flow fields exiting the GDL are described by a parametric stochastic model. This direct stochastic modeling approach gives a deeper insight into the spatial structure of the gas flow fields gained by LB simulations and it allows to quantitatively analyze the quality of gas supply, e.g., to characterize size, magnitude and arrangement of regions with high gas supply. The gas flow field at the GDL exit are described by unions of Gaussian bells, where the locations of the bells are modeled by suitable

point processes. For each binder morphology, the stochastic gas flow model is fitted to the fields computed by the LB method. Subsequently, we use the gas flow model to analyze the influence of binder morphology on gas flow by a *parametric comparison*. More precisely, the differences of the model parameters are related to differences in the structure of the gas flow fields in dependence of the binder morphology. As a result, we e.g. obtain that the total intensity of center points of bells decrease for more clustered binder morphologies, which indicates that regions with high gas supply decrease for this type of binder. Furthermore, by means of our stochastic gas flow model, the gas supply can be predicted for further binder morphologies with low computational efforts. It is preferable that the binder does not build large clusters. In this way, the understanding of the relationship between binder morphology and quality of gas supply of electrodes managed by the GDL is significantly improved.

The paper is organized as follows. Section 2 briefly describes the stochastic microstructure model, the LB method and the simulation framework of this paper. In Section 3, quality criteria evaluating the gas supply of GDL are introduced and subsequently correlated to the binder morphologies. Section 4 establishes a direct stochastic model describing the gas flow field exiting the GDL in dependency of the binder morphology. Finally, Section 5 concludes the paper and gives an outlook to possible future research.

## 2 Model Description and Simulation Framework

The supply of electrodes with gases is one of the main tasks of GDL. Thus, in this paper the influence of binder in Toray 090 GDL (belonging to the class of paper-type GDL) on single phase, single component gas flow is investigated. The basic idea is to consider a stochastic microstructure model which is able to generate a large variety of synthetic, but realistic paper-type GDL on the computer. On these synthetic structures, gas flow simulations are accomplished by the LB method. The outcome of the LB simulations are analyzed, evaluated and correlated with the corresponding binder morphology. We begin by introducing the stochastic microstructure model for paper-type GDL and the LB method used in this paper.

## 2.1 Stochastic 3D Microstructure Model

Paper-type GDL consist of straight carbon fibers and binder which agglutinates the fibers, see also Figure 2. Note that the fibers of paper-type GDL mainly run in horizontal direction. In<sup>29</sup>, a stochastic model for the 3D microstructure of this kind of paper-type GDL has been introduced which is shortly presented in the following.

### 2.1.1 3D Model for Systems of Carbon Fibers

The carbon fiber system of paper-type GDL is modeled by a multi-layer approach<sup>29</sup>, that is, a stack of independent thin layers, where each single layer is modeled by a planar Poisson line tessellation (PLT)<sup>31</sup>. Note that a planar PLT  $\Xi$  is defined as the union of random lines  $\ell_{(D_i, M_i)} = \{(x, y) \in \mathbb{R}^2 : x \cos M_i + y \sin M_i = D_i\}$ , i.e.,  $\Xi = \bigcup_{i=1}^{\infty} \ell_{(D_i, M_i)}$ , where  $\{D_i : i \geq 1\}$  is a homogeneous Poisson process in  $\mathbb{R}$  with some intensity  $\lambda_f > 0$  and  $M_i \sim U(0, \pi)$  for  $i = \{1, 2, \dots\}$  is a sequence of uniformly distributed random variables on the interval  $[0, \pi]$ . Alternatively, the PLT  $\Xi$  can be described by the cells  $\Xi_1, \Xi_2, \dots$  generated by the underlying line system. Since the fibers in GDL are 3D cylinders, each line of the PLT is dilated using a 3D sphere with the origin as center and some radius  $r_f > 0$ . Note that the parameters of the stochastic microstructure model for the fiber-system are given by the number  $n_\ell$  of fiber layers, the intensity  $\lambda_f$  of fibers within a single layer and the radius  $r_f$  of fibers. The parameters are fitted to resemble carbon fibers of a Toray 090 GDL. Realizations drawn from this fiber model are 3D images which can be given in arbitrarily large observation windows.

### 2.1.2 Modeling of Binder

Paper-type GDL additionally comprise binder, which has an essential influence on transport processes through the material, since it can block many paths through the pore phase, see Figure 2 (a). Thus, the binder is included into the microstructure model for the fiber system presented in Section 2.1.1 by a so-called *Bernoulli filling*, where to each cell  $\Xi_i$  of each layer, a Bernoulli distributed random number  $b \in \{0, 1\}$  with parameter  $p > 0$  is assigned. If the mark  $b$  of a cell is equal to 1, the cell is filled with binder, either completely or partially depending on the binder radius  $b_r$ , see Figure 3. For  $b_r \in [0, \infty)$  all voxels located in the interior of the cell with a distance smaller than  $b_r$

to the boundary are defined as binder. In particular, if  $b_r = \infty$  the cell is completely filled with binder. The binder model is uniquely determined by the volume fraction  $\nu_B$  of binder to be included into the fiber system and by the binder radius  $b_r$ . Moreover, the filling probability  $p$  can be calculated given the binder radius  $b_r$  and the volume fraction  $\nu_B$  of binder. A detailed discussion of the binder model can be found in<sup>29;32</sup>. The complete model for paper-type GDL has been successfully validated against experimental 3D image data of Toray 090 GDL<sup>29</sup>. Figure 2 shows the good optical resemblance of experimental and simulated data.

## 2.2 Numerical Calculation of Mass Transport

Using the LB method the numerical simulation of single phase, single component flow (i.e., gas transport) through the GDL is performed. Effective structural parameters can be obtained from the resulting flow fields<sup>33-35</sup>.

### 2.2.1 Lattice-Boltzmann Method

The principle idea of LB method is based on the kinetic gas theory. First of all, on the atomistic level one can look for the probability  $f(\vec{x}, \vec{p}, t)$  of finding a molecule around position  $\vec{x}$  at time  $t$  with momentum  $\vec{p}$  which leads to the Boltzmann equation<sup>36</sup>:

$$\frac{\partial f}{\partial t} + v \nabla f = Q . \quad (1)$$

with the macroscopic flow velocity  $v$ . In this equation,  $Q$  denotes the collision integral which cannot be solved in the general case. The idea to simplify the collision integral for cases where the system is not too far away from the Maxwellian distribution was proposed by Bhatnagar, Gross, and Krook in 1954<sup>37</sup> which leads to the BGK approximation of the Boltzmann equation

$$\frac{\partial f}{\partial t} + v \nabla f = -\omega (f - f^{(eq)}) , \quad (2)$$

where the collision integral  $Q$  from Eq. (1) is replaced by a relaxation term.  $\omega$  specifies the molecular collision frequency which depends on density and

temperature of the gas. Furthermore, the equation is discretized to a regular lattice and normalized by space and time. The resulting (normalized and discretized) equation is given by

$$F_i(x + c_i \Delta t, t + \Delta t) - F_i(x, t) = -\omega \left( F_i - F_i^{(eq)} \right) . \quad (3)$$

The  $c_i$  are reference velocities on a regular lattice. They are constant for a particular discretization scheme. In our case, we use as regular lattices the D3Q19 scheme. D3Q19 specifies a three dimensional regular lattice with 19 neighbored nodes ( $i = 0, \dots, 18$ ) participating on the discretized equation. The result of LB simulation is a 3D velocity field  $V$  given on a 3D grid, i.e., each voxel of the 3D grid contains a 3D velocity vector, where the vector represents the averaged direction and velocity of the gas flow in the corresponding voxel.

### 2.2.2 Boundary Conditions

The simulations were performed in the through-plane direction, i.e., we consider gas flow from the gas channel to the electrode, perpendicular to the membrane. Due to the stochastic nature of the microstructure model with its infinitely long fibers as explained in Section 2.1, wall boundary conditions at the boundaries of the simulation domain are assumed. In this way four sides of the cuboid representing the simulation domain are well defined. The upstream boundary in front of the transport direction are specified with a given velocity profile. The velocity of the gas flowing into the GDL is obtained from the amount of converted mass via Faraday's law. This specifies only a mean value of the gas which does not hold locally at every point of the GDL. For this reason a simulation frame was introduced which allows to specify the velocity profile upstream from the corresponding irregular boundary of the GDL. Free space is added to the simulation domain to allow the gas flow to rearrange according to the irregular stochastic structure where the gas enters the GDL (Figure 4). It was found that at least 5 voxels were needed upstream to ensure undisturbed flow at the boundary where the gas enters the GDL. In our simulations 10 voxels were taken for this area from conservative reasons. The downstream procedure is applied in an analogous way. Free space is added behind the GDL of the same size as before. Figure 4 depicts the situation. The boundary condition at the outlet is a constant pressure, also known as outflow boundary condition.

## 2.3 Simulation Framework

Recall that our goal is to study the influence of binder morphology in GDL on the goodness of gas supply of electrodes with respect to its spatial homogeneity. Therefore, we generate virtual, but realistic GDL microstructures with different binder morphologies and subsequently analyze the gas transport via the LB method within these structures, see Figure 1. More precisely, we choose all parameters of the stochastic microstructure model proposed in<sup>29</sup> in order to describe real Toray 090 GDL, except the binder radius  $b_r$  (or the filling probability  $p$ , respectively). In particular, we set the intensity of fibers within single layers  $\lambda_f = 0.025$ , the radius of fibers  $r_f = 3.75 \mu\text{m}$ , the volume fraction of binder  $\nu_B = 0.05$ , and the number of fiber layers  $n_\ell = 26$ . In the present paper, five different binder radii  $b_r \in \{6, 18, 30, 40, \infty\}$  (corresponding to  $p \in \{0.555, 0.116, 0.081, 0.063, 0.059\}$ ) are considered. The respective microstructures are visualized in Figures 3 and 5. In the following, we denote the synthetic morphologies with different binder radii by binder types A, . . . , E, see Table 1. To enhance the accuracy for the statistical analysis accomplished in this paper, for each type of binder morphology, 25 independent samples of 3D microstructures are drawn from the stochastic GDL model. Thus, in summary, 125 simulations of virtual (but realistic) paper-type GDL build the data base for the simulation of mass transport. Each sample is represented by a 3D image stack of size  $130 \times 512 \times 512$  with cubic voxels of  $(1.5 \mu\text{m})^3$ . This leads to an overall thickness of the simulated GDL of  $195 \mu\text{m}$  which is equivalent to 130 consecutive 2D slices with size  $768 \times 768 \mu\text{m}^2$ . The size of the 3D synthetic structures (i.e.,  $195 \times 768 \times 768 \mu\text{m}^3$ ) was chosen such that it coincides with typical domains of experimental (tomographic) 3D image data. Note that the expected volume fraction  $\nu$  of the solid phase of the simulated structures is fixed to  $\nu = 1 - \epsilon = 0.22$  for all the considered binder types, with porosity  $\epsilon$ .

Using the LB method, gas flux in through-plane direction via the pore phase of these microstructures is computed. The gas flow accounts for characteristic operating conditions of a HT-PEFC, which are summarized in Table 2. With the given parameter constellation the Reynolds number is  $\text{Re} \approx 4 \cdot 10^{-4}$  related to the fiber diameter. In this case the flow is classified as creeping flow since  $\text{Re} \ll 1$ , see also<sup>38</sup>.

In summary, we end up with 125 gas flow simulations (25 per binder type) on the virtually generated structures, which are computed by the LB method. The results of these simulations build the data base for the analysis and

evaluation of gas supply of electrodes by Toray 090 GDL with respect to its binder morphology.

## 2.4 Accuracy of Simulation Study

In this section, we validate the gas flux simulations computed for the virtually generated GDL structures as described in Sections 2.2 and 2.3. More precisely, we compare permeabilities measured for Toray 090 GDL which are stated in literature with the results obtained by the gas flux simulations on the virtual microstructures.

To best of the authors' knowledge, the literature about measurements of porosity and permeability for Toray 090 GDL is scarce. Gostick et al.<sup>39;40</sup> presented measurements on GDL materials including Toray 090. Hussaini et al.<sup>4</sup> measured relative permeabilities of several GDL materials, also including Toray 090. Recent measurements are presented in<sup>41;42</sup>. The porosity of Toray 090 considered in these papers is ranging from 72 % to 80 % and the thickness of the paper-type GDL is specified from 190  $\mu\text{m}$  to 290  $\mu\text{m}$  which coincides very well with the corresponding (fixed) values of our simulation study (i.e., porosity of 0.78 and thickness of 195  $\mu\text{m}$ ). Moreover, the through-plane permeability ranges from 4.4 to 12.4  $\mu\text{m}^2$ . The large deviations of these values especially of the Toray 090 material were already reported by Hussaini<sup>4</sup>, who also stated the different operating conditions (e.g. compression) of the measurements. Note that a higher degree of compression leads to lower permeabilities as shown in<sup>26;41;43;44</sup>. For this reason the values given in Table 3 might deviate from calculated permeabilities on uncompressed geometries. The measured permeabilities reported by Hussaini et al.<sup>4</sup> are also listed in Table 3.

Effective permeabilities and tortuosities obtained from our transport simulations are shown in Figure 6. Moreover, the means and standard deviations of these values with respect to the different binder types are listed in Table 4. Although it is not possible to obtain a perfect match with the values of literature (due to the large deviation of measured permeabilities), the comparison of our calculated numbers and the measured values from literature shows that they are in the same range. This suggests that the combination of the stochastic microstructure model with LB gas flow simulations describe gas flow within the GDL in a realistic way.

Additionally, the simulated permeabilities show a large variation for each binder type which is caused solely by the stochastic spread in the generated microstructures. But nevertheless, considering the mean values of Table 4 a clear influence of the binder model on the permeabilities can be observed.

### 3 Quality Criteria for Mass Transport

For a high power conversion rate of PEFC, it is desirable that the exiting gas flux after crossing the GDL is as homogeneously distributed as possible, i.e., there should not occur any regions at the interface between the GDL and electrodes where little or no gas arrives. In case of inhomogeneous gas flow, electrochemical reactions do not take place at location where no gas arrives which leads to low conversion rate of hydrogen. The standard proceeding in analyzing the mass transport through porous media is to compute characteristics like permeability, tortuosity or diffusibility which are well-known indicators for mass transport. However, these characteristics do not quantify the *homogeneity* of gas flow at the exit of the GDL. Since the main task of the GDL is a possibly homogenous gas supply of the electrodes, methods for characterization of the *local* gas flow in terms of homogeneity are required. The introduction of such characteristics lead to criteria for the quality of gas flow through the GDL.

#### 3.1 Gas Flow Field

We now introduce characteristics evaluating the quality of gas supply of electrodes by the GDL. More precisely, we introduce two characteristics evaluating the *homogeneity* of the exiting gas flux after crossing the GDL. These characteristics are functionals of gas flow simulations computed by the LB method. Note that the result of LB simulations are velocity fields  $V$  on the voxel grid of the input image, i.e., in our case the velocity fields are given by  $V : [0, 129] \times [0, 511] \times [0, 511] \rightarrow \mathbb{R}^3$ , see Section 2.2.1.

The voxel  $(129, y, z)$  located at the top layer of the velocity field  $V$  (i.e., at the exit of the GDL) contains information about the mass of gases reaching the electrode at each time point  $t > 0$  at location  $(y, z)$ , i.e., the voxel contains information about the gas flow. Because the density of the gas in the free space behind the GDL is almost homogeneous, the first component

( $u$ -values) of the velocity vectors in  $V(x, y, z) = (u, v, w)^\top$  is proportional to the mass of gases reaching the location  $(x, y, z)$  at each time point  $t > 0$ . The scalar field of the  $u$ -values located at the top layer of the GDL is denoted by  $T : [0, 511] \times [0, 511] \rightarrow \mathbb{R}$ ,  $T(y, z) = (1, 0, 0) \cdot V(129, y, z)$  in the following. To get an idea of the structure of such a gas flow field  $T$ , see Figure 7, where a synthetic paper-type GDL and its corresponding field  $T$  are plotted. Thereby, in Figure 7, the dependency of the gas flow field  $T$  on the microstructure of the synthetic GDL can be nicely seen. In Figure 8, gas flow fields are visualized for five different microstructures (computed according to the simulation framework described in Section 2.3). Since the gas flow field  $T$  is gained by LB simulations on random (stationary) 3D microstructures of GDL,  $T$  can be interpreted as a (stationary) *random field*<sup>45</sup>, i.e., for each  $(y, z)$  the quantity  $T(y, z)$  is a random variable, where the random variables  $T(y, z)$  and  $T(y', z')$  for different locations  $(y, z)$  and  $(y', z')$  might be correlated in space. Note that, roughly speaking, a random field is stationary if its mean and variance do not change depending on the position.

### 3.2 Variability of Gas Flow

It is far from being straightforward how to evaluate the spatial homogeneity of the mass transport at the exit of the GDL (described by the gas flow field  $T$ ). In the ideal case with respect to uniform mass transport, the gas flow field  $T$  is a constant scalar field within the pore space, i.e.,  $T(y, z) \equiv c$  for some  $c \in \mathbb{R}$  and for all  $(y, z)$  which are located within the pore phase. If there exist inhomogeneities, i.e., deviations from the mean value of  $T$ , it is desirable that the sum of all deviations is as small as possible. (Note that existing inhomogeneities are stationarily distributed in space since the underlying stochastic microstructures are stationary.) Besides the total deviation, it is desirable that the *size*, *magnitude* and *intensity* of the inhomogeneities are as small as possible.

Note that the mean values of gas flow  $T$  in the exit plane of the GDL are constant for all regarded scenarios of the present simulation study if the domain size of  $T$  is chosen large enough. But since we consider the gas flow  $T$  in rather small observation domains, it may occur that the mean values vary. To account for the possibly varying mean values of gas flow, we introduce characteristics evaluating the gas supply of electrodes independently of these mean values.

We therefore consider the following two characteristics. As a measure of global variability, the (empirical) coefficient of variation

$$\rho_T = \frac{\sqrt{\frac{1}{n-1} \sum_{i=1}^n (x_i - \frac{1}{n} \sum_{i=1}^n x_i)^2}}{\frac{1}{n} \sum_{i=1}^n x_i} \quad (4)$$

is considered, where  $\{x_1, \dots, x_n\} = \{T(y, z), y, z \in \{0, \dots, 511\}\}$ . The coefficient of variation  $\rho_T$  is a normalized measure of dispersion from the mean value of the gas flow field  $T$ . It is normalized such that it does not depend on the mean value of  $T$ .

Furthermore, the function  $\gamma_T : [0, \infty) \rightarrow [0, \infty)$  is considered describing the variation in space (i.e., magnitude, size and arrangement of inhomogeneities) of  $T$ , which is given by a normalized version of the so-called empirical variogram<sup>45</sup>, i.e.,

$$\gamma_T(r) = \frac{\sqrt{\frac{1}{|n(r)|} \sum_{(i,j) \in n(r)} (x_i - x_j)^2}}{\frac{1}{n} \sum_{i=1}^n x_i}, \quad (5)$$

where  $n(r)$  denotes the set of pairs  $i, j \in \{0, \dots, 511\}$  such that  $|x_i - x_j| = r$ , and  $|n(r)|$  is the number of pairs of the set  $n(r)$ . The normalized empirical variogram specifies the dependency of values  $T(u, v), T(w, q)$  of point pairs  $(u, v), (w, q)$  with a specified distance of  $r = |(u, v) - (w, q)|$ . Important characteristics of the variogram are the sill  $S$  which is the limit of the variogram if  $r$  tends to infinity and the range  $R$  defined by the distance when the variogram first reaches 95% of the sill. The sill  $S$  is equal to the coefficient of variation  $\rho_T$  of  $T$ , where the range  $R$ , roughly speaking, stands for the distance of point pairs  $(u, v), (w, q)$  whose values  $T(u, v), T(w, q)$  are dependent of each other. More precisely, points that are close to each other will generally have a stronger correlation in their values than those farther apart. The range  $R$  gives the maximal distance between pairs of points where a correlation of their values is significant. For more information about the variogram the reader is referred to<sup>45</sup>. Furthermore, the course of the normalized variogram for gas flow fields  $T$  depends on the magnitude, size and arrangement of inhomogeneities. In particular, larger magnitudes lead to a larger sill  $S$  and larger sizes to a larger range  $R$ .

Since it is preferable to characterize the spatial arrangement of inhomogeneities by a single value, the following global characteristic is considered. Let  $g_T$  be the integral over the normalized empirical variogram  $\gamma_T(\cdot)$  from 0 to the range  $R$ , i.e.,

$$g_T = \int_0^R \gamma_T(r) dr \quad (6)$$

Note that  $g_T$  is large if the range  $R$  and/or the sill  $S$  reaches large values. Considering the case that, both,  $R$  and  $S$  are small, then  $g_T$  will be small too. This is desirable since a small range  $R$  indicates that the sizes of inhomogeneities are small and a small sill  $S$  stands for a small global variability which can only be the case if the magnitude and size of the inhomogeneities of  $T$  are small. In general,  $g_T$  depends on the length of integration interval  $[0, R]$ , but also on the values of  $\gamma_T(\cdot)$  which are by trend large if  $S$  (being the limit of  $\gamma_T(r)$  as  $r \rightarrow \infty$ ) is large.

Recall that uniform mass transport for the gas supply of electrodes by the GDL is preferred. Thus, smaller values of  $g_T$ ,  $\rho_T$  evaluate the scalar field ‘better’ and indicate a better gas supply by the GDL.

### 3.3 Statistical Analysis of the Quality of Gas Supply

In Section 3.2, criteria evaluating the quality of gas supply of electrodes by the GDL were introduced. We apply these quality measures to all mass transport simulations via the LB method for the virtual microstructures of paper-type GDL drawn from the stochastic simulation model, see Section 2. Subsequently, we correlate the values of the quality measures with the binder morphology controlled by the binder radius  $b_r$  (or filling probability  $p$ , respectively).

#### 3.3.1 Means and Fluctuations of Quality Measures

Table 5 shows that with increasing binder radius  $b_r$ , the mean values of all characteristics (coefficient of variation  $\rho_T$ ,  $g_T$  and range  $R$ ) monotonously increase with increasing binder radius. This strongly suggests that the quality of gas supply decreases with increasing binder radius. Thus, there is strong evidence that large clusters of binder which hamper the gas flux, are unfavorable for a homogeneous gas supply. Note that the different binder types A, B, C, D, and E have been realized such that the resulting (synthetic) paper-type GDL exhibit a constant volume fraction of the solid phase (i.e., fibers plus binder).

What is striking, however, are the relatively large fluctuations of the values of  $\rho_T$  and  $g_T$  for each given binder type as displayed in Figure 9. Note that the microstructure of synthetic paper-type GDL is random which is captured

by the stochastic microstructure model explained in Section 2.1. Thus, one can expect some natural fluctuations regarding the microstructure and subsequently, also variations regarding the values of the quality measures. Nevertheless, if the size of the synthetic microstructures (observation window) is large enough these variations will balance and thus, will be more or less the same for each (independent) replication of a given binder type. In short, a large image is beneficial for high accuracy of computed characteristics and this accuracy can be increased by either increasing the volume of the image or by averaging over an increasing number of replications (i.e., considering several independent 3D images). In our case, from Figure 9 we see that - although the considered image is relatively large ( $195 \mu\text{m} \times 768 \mu\text{m} \times 768 \mu\text{m}$ ) - a single 3D image is not enough to measure effects of binder morphology accurately. In fact, if one considers only a series of single images for the different morphologies, one might even obtain, due to the large variations, a wrong trend, e.g., that large binder radii are preferable for a homogeneous gas flux.

This emphasizes the absolute necessity of considering a sufficiently large number of 3D images per binder type to obtain accurate results when one performs a quantitative analysis.

The acquisition of a sufficiently large number of experimental (tomographic) 3D images, however, is expensive in terms of financial and time resources. In our case, this situation has been remedied by the stochastic model, where synthetic microstructures can be efficiently generated at almost no costs. In addition, by parallelizing the computation of the LB method on super computers, it is possible to obtain gas flow simulations in relatively short time.

### 3.3.2 Influence of the Top Layers

Considering the histograms of  $\rho_T$  and  $g_T$  in Figure 9, we see that the fluctuations of these values per binder type are rather large (i.e., we can observe a large width of the histograms). As discussed in Section 3.3.1, these strong deviations would decrease for larger observation windows. However, in addition to this, the question arises which morphological features of the GDL microstructure are responsible for the large variability of the quality measures for each binder type.

Thus, for each binder type, we aim to detect structural characteristics, which

lead to the fluctuations of the values of  $\rho_T$  and  $g_T$ , respectively. For brevity, we only consider the variability of the coefficient of variation  $\rho_T$ , since the investigation of  $g_T$  leads to analogous results. Due to the chosen size of the observation window and the stochastic nature of the microstructure model (constructed by a multi-layer approach), the volume fraction of the individual fiber layers plus the binder therein is subject to fluctuations. Furthermore, it is clear that the layers located at the top of the synthetic GDL are more important for the variability of the gas flow field at the exit of the GDL. Thus, our assumption is that the volume fraction averaged over the top layers of the synthetic GDL highly influences the value of the variation coefficient  $\rho_T$ .

It turns out that the volume fraction  $\nu_i$  of the solid phase (i.e., fibers and binder) of the  $i$  top layers is mainly responsible for the variability of  $\rho_T$  for a fixed binder type. Recall that the virtual GDL consists of  $n_\ell = 26$  layers. To determine the number of top layers  $i$  which are closely related to the value  $\rho_T$ , we maximize the Pearson correlation coefficient  $cor(\rho_T, \nu_i) \in [-1, 1]$  with respect to the number of top layers  $i$ , since the correlation coefficient is a measure of the strength of linear dependence of  $\nu_i$  and  $\rho_T$ <sup>46</sup>. The closer  $cor(\rho_T, \nu_i)$  is to 1 the stronger is the linear dependency of  $\rho_T$  and  $\nu_i$ . In Table 6, the maximized correlation coefficient with respect to the number of top layers  $i$  (i.e.,  $\max_{i \in \{1, \dots, 26\}} cor(\rho_T, \nu_i)$ ) as well as the number of top layers  $i$  with the maximum correlation coefficient (i.e.,  $\arg \max_{i \in \{1, \dots, 26\}} cor(\rho_T, \nu_i)$ ) are listed. Furthermore, in Figure 10 the characteristics  $\nu_{\arg \max_{i \in \{1, \dots, 26\}} cor(\rho_T, \nu_i)}$  and  $\rho_T$  are plotted against each other for binder types A and C. Note that the remaining binder types show the same behavior. We can clearly see that the value of  $\nu_i$  gives a good prediction of the corresponding value of  $\rho_T$ . Moreover, it also turns out that number  $i$  of most relevant top layers increases for increasing binder radius  $b_r$ . This leads to the conclusion that the influence of binder on the homogeneity of gas flow at the GDL exit is higher for larger binder clusters.

## 4 Direct Stochastic Modeling of Gas Supply

In this section, we develop a parametric stochastic model for the gas flow field  $T$  at the exit of the GDL. By means of this stochastic model it is possible to realistically mimic the results of the LB simulations regarding gas flow at the exit of the GDL with negligible computational effort, i.e., the gas flow field  $T$  computed by LB and the corresponding field  $T_S$  generated by the stochastic model, will exhibit the same structure in terms of magnitude, size

and spatial arrangement of inhomogeneities of the gas flux.

Moreover, this direct stochastic modeling approach has further benefits. First, the stochastic model gives a deeper insight into the geometric structure of gas flow fields at the exit of the GDL. In this way, it allows to better compare structural differences in the gas flow fields for GDL with different binder morphologies. More precisely, the stochastic model allows us to quantitatively analyze the gas supply, e.g., to characterize magnitude, size and arrangement of regions with high gas supply at the GDL exit.

In addition to this, we can apply the stochastic gas-supply model in a way that allows to *predict* the gas flow field  $T$  at the GDL exit for binder morphologies which have not been considered so far (i.e., for  $b_r \notin \{6, 18, 30, 40, \infty\}$  without performing expensive LB simulations).

Our goal is to describe the field  $T$  of exiting gas flows after crossing the GDL for the binder types A, B, C and E by a spatial stochastic model. Note that we do not take binder type D into account for model fitting, since we will use it for the validation of the predictive capability of our stochastic model, i.e., we compare the gas flow fields predicted by our model to the fields gained by the LB method as described in Section 2.

To get an idea which class of stochastic models might be suitable to describe the gas flow fields  $T$  for all different binder types  $A, B, C, E$ , it is useful to re-consider the results visualized in Figure 8. This figure suggests that a gas flow fields resemble a system of Gaussian bells,

Thus, for modeling the field  $T$  of exiting gas flows we consider unions of Gaussian bells, with random locations and heights. In a first step, a suitable 2D point-process model is chosen which describes the locations of the Gaussian bells, see Figure 11 (a). Subsequently, each point of the point process is marked by a random height, as displayed in Figure 11 (b). Finally, to each marked point, we associate a truncated Gaussian bell, where the variance and the range of the bell can be adjusted appropriately, see Figure 11 (c). Note that the heights of the points are the maximum of the bells. By the union of the bells, the stochastic model is given describing the gas flow field  $T$  after crossing the GDL.

## 4.1 Modeling the Locations of Local Maxima

We consider a suitable 2D point-process model which is flexible enough to describe the locations of bells for all binder types A, B, C, E. As mentioned before, binder type D is not taken for fitting but used for validation instead. In this context, note that the gas flow fields  $T$  are given as 2D pixel images, where the value of a pixel indicates the gas flow at the corresponding location. Our idea is to interpret the local maxima of these 2D images as the center points of the truncated Gaussian bells. This assumption is reasonable since the local maxima in the 2D images indicate areas with peak gas flux. Thus, local maxima of the gas flow field have a minimum distance of  $r_h = 3 \mu\text{m}$  from each other since the maxima cannot be located in neighboring pixels and the pixel size is equal to  $1.5 \mu\text{m}$ . This minimum distance  $r_h$  is called *hardcore distance* and it is included into the model.

In order to model the locations of bells, we consider a class of point processes which is build by a *modulated dominance-competition* principle. In this way a hardcore distance  $r_h$  (i.e., a minimum distance between points) as well as clustering and repulsion effects of points can be included into the model.

The idea of modulated dominance competition consists of a two-stage approach where in a first step a random set  $\Xi_A$  (avoidance set) is generated in which no point is allowed to be located. Then, in the second step, we release points in the complement of the avoidance set  $\Xi_A$  according to a so-called dominance-competition principle.

The avoidance set  $\Xi_A$  is given by a union of random circles, i.e.,

$$\Xi_A = \bigcup_{n=1}^{\infty} b(P_n, r_A) \quad (7)$$

where the midpoints  $P_n$  of the circles  $b(P_n, r_A)$  form a stationary Poisson process  $\{P_n\}$  in  $\mathbb{R}^2$  with some intensity  $\lambda_P > 0$ , and the radius of the circles is some constant  $r_A > 0$ . The benefit of including the avoidance set  $\Xi_A$  into the model is that in this way we are able to get areas where no or only few gas particles will flow.

In the next step, we consider a stationary dominance-competition point process  $\{S_n\}_{n \geq 1}$  in  $\mathbb{R}^2$  with some intensity  $\lambda_S > 0$  and random radii  $R_n$ . Note that by an appropriate choice of the distribution of the random radii  $R_n$ , the distances between pairs of points can be controlled efficiently. We consider

a shifted Gamma distribution, i.e.,  $R_n = G_n + r_h$ , where  $G_n$  is a Gamma-distributed random variable with some mean  $r_1$  and variance  $r_2$ . For further information about the dominance-competition model the reader is referred to<sup>47–49</sup> and the references therein.

Assuming that the point processes  $\{P_n\}$  and  $\{S_n\}$  are independent, the modulated dominance-competition model  $\{M_n\}$  is defined by  $\{M_n\} = \{S_n\} \cap \Xi_A^c$ , where  $\Xi_A^c$  denotes the complement of  $\Xi_A$ . Thus, in  $\{M_n\}$  only those points of  $\{S_n\}$  are taken into account being not located in the avoidance set  $\Xi_A$ . By  $\lambda > 0$ , we denote the required intensity of  $\{M_n\}$ . Moreover, the intensity  $\lambda_S$  of the dominance-competition model  $\{S_n\}$  can be determined by simulation experiments provided that the parameter vector  $(\lambda, \lambda_P, r_A, r_1, r_2, r_h)$  of the modulated dominance-competition model  $\{M_n\}$  is given.

In this way, we succeed in generating areas (given by  $\Xi_A$ ) where low or no gas flow occurs, whereas the clustering and repulsion of local maxima is nicely controlled by the dominance-competition model  $\{S_n\}$ . Thus, the modulated dominance-competition model  $\{M_n\}$  can be described by five parameters:  $\lambda_S, \lambda_P, r_A, r_1, r_2, r_h$ . Note that instead of  $\lambda_P$ , the area fraction  $\nu_A$  of  $\Xi_A$  can be considered which is given by  $\nu_A = 1 - \exp(-\lambda_P \pi r_A^2)$ .

#### 4.1.1 Model Fitting

The parameters of the modulated dominance-competition model are fitted to the point pattern of local maxima extracted from the gas flow fields for each group of binder separately.

The intensity  $\lambda$  of the stationary point process  $\{M_n\}$  can be easily estimated by

$$\lambda = \frac{\text{total number of local extrema in the 25 realizations per binder radius}}{25 \text{ times the volume of sampling window}}.$$

Moreover, the hardcore distance  $r_h$  is equal to 3  $\mu\text{m}$ . The remaining four parameters  $(\nu_A, r_A, r_1, r_2)$  are estimated using the minimum-contrast method with respect to the pair-correlation function  $g$  of  $\{M_n\}$ . Note that  $g(r)$  is proportional to the relative frequency of point pairs with distance  $r > 0$  from each other<sup>31</sup>. More precisely,  $(\nu_A, r_A, r_1, r_2)$  are chosen such that the discrepancy  $\int_{15}^{75} (\bar{g}(x) - \bar{g}_{(\nu_A, r_A, r_1, r_2)}(x))^2 dx$  between the pointwise averaged (empirical) pair-correlation function  $\bar{g}$  over the 25 realizations of sets of local extrema and its simulated counterpart  $\bar{g}_{(\nu_A, r_A, r_1, r_2)}$  drawn from the modulated

dominance-competition model  $\{M_n\}$  is minimized. Note that the values of  $g(r)$  for  $r < 15 \mu\text{m}$  can be seen as estimation artifacts since there exist only few point pairs with such a short distance to each other. In Table 7, the fitted parameters of the point process  $\{M_n\}$  for the different binder types are listed. Figure 12 (a) shows that the modulated dominance-competition model  $\{M_n\}$  fitted to the local extrema of each binder type A, B, C, and E excellently reflects the averaged empirical pair-correlation functions. The same is true for other image characteristics which have not been used for model fitting, see Section 4.1.2 below.

#### 4.1.2 Model Validation

To check if the fitted point-process model  $\{M_n\}$  reproduces the observed point pattern of local extrema sufficiently well, the accordance of a further important structural characteristic of irregular point patterns, the histogram of spherical contact distances, is investigated. It is defined as the histogram of the distance from a randomly chosen location in the observation window to the closest point of the point process<sup>31;47</sup>. Plots of these histograms are shown in Figure 12 (b), for both the extracted local extrema and simulated point patterns, where a very good coincidence is observed. Moreover, the extracted and simulated point patterns themselves are in a good optical accordance, see Figure 13.

## 4.2 Modeling the Heights of Local Maxima

In the next step, to each point  $M_n$  of the modulated dominance-competition model  $\{M_n\}$  we assign a random height  $H_n$  which represents the height of the truncated Gaussian bell to be constructed. We choose  $H_n$  as independent and identically distributed random variables following a shifted, and truncated Gamma distribution, i.e.,  $H_n \sim g_{min} + \Gamma(g_1, g_2, g_{max})$  where  $g_{min}$  shifts the Gamma distribution and  $g_{max}$  truncates it, i.e., realizations of  $H_n > g_{max}$  are rejected. Moreover,  $g_1$  denotes the shape and  $g_2$  the scale parameter of the Gamma distribution. The truncation is reasonable since the maximum gas flow should be finite.

For parameter fitting, we first choose the values of  $g_{min}$  and  $g_{max}$ , respectively, putting them equal to the minimal and maximal values of the extracted local extrema per binder type. The parameters  $(g_1, g_2)$  are estimated using the

minimum-contrast method minimizing the Kolmogorov distance between the empirical distribution functions computed for the observed values of local extrema and simulated values drawn from the shifted and truncated Gamma distribution, see Figure 12 (right). The fitted values are listed again in Table 7. The mean values and standard deviations of the heights of the fitted distributions are given by  $0.0032 \pm 0.0029$  for binder type A,  $0.0031 \pm 0.0031$  for binder type B,  $0.0032 \pm 0.0031$  for binder type C, and  $0.0031 \pm 0.0036$  for binder type E.

### 4.3 Modeling the Gas Flow Field

So far in Sections 4.1 and 4.2, we have introduced a marked dominance-competition model  $\{(M_n, H_n)\}$  describing the local extrema and their heights of the field  $T$  of gas flows. Next, we assign to each marked point  $(M_n, H_n)$  a truncated Gaussian bell, where the maximum height of the bell is equal to  $H_n$  and the parameters  $\sigma$  (standard deviation) and  $\kappa$  (range) control the width and truncation of the bell. More precisely, the truncated Gaussian bell  $G_b(M_n, H_n, \sigma, \kappa) \in \mathbb{R}^3$  is defined by

$$G_b(M_n, H_n, \sigma, \kappa) = \{(x, y, f(x, y))^\top \in \mathbb{R}^3 : f(x, y) = H_n \times \exp\left(-\frac{(x-M_{1,n})^2+(y-M_{2,n})^2}{2\sigma^2}\right) \mathbb{1}_{|(x,y)^\top - M_n| \leq \sigma\kappa}\}, \quad (8)$$

where  $|(x, y)^\top - M_n|$  denotes the Euclidean distance between  $(x, y)^\top$  and  $M_n = (M_{1,n}, M_{2,n})$ .

The complete model  $\Psi$  describing the gas flow field  $T$  is then given by

$$\Psi(\{M_n, H_n\}, \sigma, \kappa) = \bigcup_{n=1}^{\infty} G_b(M_n, H_n, \sigma, \kappa). \quad (9)$$

#### 4.3.1 Model Fitting

The stochastic model  $\Psi$  introduced in Eq. (9) depends on the marked modulated dominance-competition model  $\{(M_n, H_n)\}$  and on the parameters  $\sigma, \kappa \in [0, \infty)$ . The fitting of the parameters of  $\{(M_n, H_n)\}$  has already been discussed in Sections 4.1-4.2. We therefore focus on the estimation of  $\sigma$  and  $\kappa$ , where we again use the minimum-contrast method for the Kolmogorov distance between the empirical cumulative distribution function of all values

of the observed gas flow fields and  $\Psi(\{M_n, H_n\}, \sigma, \kappa)$  within an observation window. See Table 7 for the corresponding list of fitted parameters for the different binder types.

### 4.3.2 Model Validation

For model validation, the quality measures introduced in Section 3.1 in order to evaluate the goodness of gas supply are computed for the observed and the simulated (drawn from  $\Psi$ ) gas flow fields. More precisely, the averaged normalized variograms of observed and simulated gas flow fields are plotted in Figure 14, where the mean values and standard deviations of the coefficients of variation  $\rho_T$  are listed in Table 8. The results show that there is a very good agreement between observed and simulated data. Moreover, the visual accordance of gas flow fields gained by the LB method and drawn from the stochastic model presented in this section is also quite good, see Figure 15.

## 4.4 Prediction of Gas Flow Fields

In Section 4.3, a stochastic model has been introduced, which adequately describes the fields of gas flow for binder types A, B, C, E gained by LB simulations.

We now use this model to predict the fields of gas flow for binder radii which have not been considered so far. That means, for an arbitrary binder radius  $b_r \in [6, \infty]$  or an arbitrary filling probability  $p \in [0.059, 0.555]$  the resulting gas flow fields and thus the goodness of gas flow for all binder morphologies generated by the stochastic microstructure model for paper-type GDL described in Section 2 can be predicted. Throughout this section, we will focus on the filling probability  $p$  instead of the binder radius  $b_r$  since all possible values for the filling probability  $p$  are given in the finite interval  $[0.059, 0.555]$ , in contrast to the binder radius  $b_r \in [6, \infty]$ . Note that in general, the filling probability  $p$  can take an arbitrary value from the interval  $[0, 1]$ . But since all other parameters of stochastic GDL model, introduced in Section 2, are kept fixed and the volume fraction of the GDL should also be constant, the filling probability  $p$  is restricted to the interval  $[0.059, 0.555]$ .

#### 4.4.1 Interpolation of Model Parameters

For the stochastic microstructure model of GDL considered in the present paper, gas flow fields have been computed using the LB method for specific binder filling probabilities  $p \in \{0.555, 0.116, 0.081, 0.059\}$  (corresponding to  $b_r \in \{6, 18, 30, \infty\}$ ). However, what is missing so far, are computations of gas flow fields for arbitrary filling probabilities  $p \in [0.059, 0.555] \setminus \{0.555, 0.116, 0.081, 0.059\}$ . We now propose a *predictive* gas flow model where we proceed as follows: Recall that for each filling probabilities  $p \in \{0.555, 0.116, 0.081, 0.059\}$ , the parameters of the stochastic model  $\Psi$  (describing the gas flow field) have been fitted. Considering the parameters of  $\Psi$  as a function of  $p$ , this provides 4 points of support for each parameter of the stochastic gas flow model  $\Psi$ . A subsequently application of (non-linear) regression models to the four points of support we obtain a parametric class of models  $\{\Psi_p, p \in [0.059, 0.555]\}$ <sup>50</sup>.

More precisely, the stochastic gas flow model  $\Psi$  is uniquely determined by 12 parameters  $c_1, \dots, c_{12}$ , where

$$(c_1, \dots, c_{12}) = (\lambda_S, \nu_A, r_A, r_1, r_2, r_h, g_{min}, g_{max}, g_1, g_2, \sigma, \kappa) \quad (10)$$

i.e.,  $\Psi = \Psi_{(c_1, \dots, c_{12})}$ . Since the parameters depends on the filling probability  $p$ , we interpret the parameter vector  $(c_1, \dots, c_{12})$  as a function of the filling probability  $p$ , i.e.,  $(c_1, \dots, c_{12})^\top : [0.059, 0.555] \rightarrow \mathbb{R}^{12}$  with

$$p \rightarrow (c_1(p), \dots, c_{12}(p)) \quad (11)$$

For each  $p \in \{0.555, 0.116, 0.081, 0.059\}$ , the parameters  $(c_1, \dots, c_{12})$  of  $\Psi_{(c_1, \dots, c_{12})}$  have been fitted which yields 4 points of support for each of the functions  $(c_1(p), \dots, c_{12}(p))$ , i.e., we obtain  $(\hat{c}_1(p), \dots, \hat{c}_{12}(p))$  for  $p \in \{0.555, 0.116, 0.081, 0.059\}$ .

The predictive model for fields of gas flow given by  $\Psi_{(c_1(p), \dots, c_{12}(p))}$  for  $p \in [0.059, 0.555]$ , where  $c_i(p) = \alpha_i \cdot p^{\beta_i} + \gamma_i$ , for some  $\alpha_i, \beta_i, \gamma_i \in \mathbb{R}$ , adequately describes the relationship between  $c_i$  and  $p$ . This can be seen in Figure 16 displaying the approximation of the points of supports by the functions  $c_i(p)$ . In Table 9 the fitted values of  $\alpha_i, \beta_i$  and  $\gamma_i$  can be found.

#### 4.4.2 Model Validation

To validate the predictive capability of the stochastic model  $\Psi_{(c_1(p), \dots, c_{12}(p))}$ , we check if the model is able to predict the fields of gas flow for the binder

type D which was not used for the fitting of  $(c_1(p), \dots, c_{12}(p))$ . Therefore, we compare the quality measures introduced in Section 3 for the gas flow fields which are gained by the LB method for binder type D (filling probability  $p = 0.063$ ) and computed for its simulated counterpart drawn from  $\Psi_{(c_1(0.063), \dots, c_{12}(0.063))}$ . In particular, the mean value (standard deviation) of the coefficients of variation for the gas flow fields of binder type D is 1.33 (0.12) (see Table 5), where its simulated counterpart is equal to 1.34 (0.08). Additionally, the averaged normalized variograms are plotted in Figure 17 (a).

Finally, for binder type D, we visually compare a gas flow field computed via the LB method and a simulated field drawn from  $\Psi_{(c_1(0.063), \dots, c_{12}(0.063))}$ , see Figure 17 (b, c). A very good agreement is found for the computed characteristics as well for the visualized fields. In summary, the stochastic gas flow model  $\Psi_{(c_1(p), \dots, c_{12}(p))}$  is capable to predict fields of gas flow at the exit of GDL with arbitrary binder radius  $b_r$ .

## 4.5 Structural Properties of Gas Flow Fields

The description of the gas flow fields by a predictive stochastic model gives a deeper insight into the structural properties of the gas flow fields. It thus allows to quantitatively analyze local properties of gas flow, e.g., to characterize magnitude, size and arrangement of regions with high gas supply.

In particular, we link the parameters of the (predictive) gas flow model given in Tables 7 and 9 with local properties of gas flow fields for different binder morphologies. Recall that the fields of gas flow are modeled by unions of truncated Gaussian bells. We concentrate on the following characteristics.

- (a) The parameters  $\kappa$  and  $\sigma$  are responsible for the width and the range of the truncated Gaussian bells. The curve progressions of both parameters indicate only insignificant differences for  $\kappa$  and  $\sigma$  for the different values of the filling probability  $p$ . This suggests that the width and the range of the inhomogeneities are invariant with respect to the size of binder radii.
- (b) Recall that the avoidance set  $\Xi_A$  indicates areas where no bells are allowed to be located. Thus, the increase of the area fraction  $\nu_A$  of  $\Xi_A$  for increasing binder radius indicates that the area of regions with no or only small gas flow increases significantly for large binder radii.

- (c) The total intensity  $\lambda$  of bells decreases for increasing binder radius. Thus, taking property (a) into account, for large radii there are fewer areas with high gas flow.
- (d) Regarding the height of the gas flows (c.f. Figure 12 (c)), we observe an increase of the maximum values  $g_{max}$  and of the variance for increasing binder radii, where the mean value of the heights remains nearly constant, see Section 4.2. Thus, for large radii, there are fewer areas of gas flow (c.f. property (c)), however, the peaks of local gas flow as well as the variability of heights are significantly increased.

## 5 Conclusion and Outlook

In this paper, we studied the influence of the binder morphology in paper-type GDL on the quality of gas supply of the electrodes. The principal idea was to generate virtual 3D microstructures representing paper-type GDL by a stochastic simulation model, where the binder morphology was modified in a systematic manner. On these structures single phase, single component gas flow was computed by the LB method. Subsequently, we introduced and analyzed quality criteria evaluating the spatial homogeneity of gas supply with respect to the binder morphology. In addition to this, the goodness of gas supply was directly analyzed by a parametrized stochastic model which describes the gas flow field at the exit of the GDL. It was found that the binder morphology has an essential influence on the quality of gas supply, where it is preferable that the binder does not build large clusters. In particular, the clusters were lower than 50  $\mu\text{m}$  which is much smaller than relevant sizes of macroscopic flow structures. The latter are typically channel widths and heights in the range of millimeters.

The presented methods build a toolbox for virtual material design in the field of creeping gas transport in complex microstructures. Not only effective parameters are calculated but also qualitative criteria of the capability of the microstructure for gas transport. Last but not least the quantitative analysis provides valuable information about the size of irregularities in the gas transport caused by the microstructure.

In a forthcoming paper, we will use the same strategy of combining stochastic and numerical methods as considered in the present paper, for the evaluation of gas flow in compressed GDL.

## Acknowledgements

This research is funded by the German Federal Ministry of Education and Research grant 03MS507. The transport simulations are running on hardware of the Jülich Supercomputing Centre.

## References

1. R. P. O'Hayre, S.-W. Cha, W. G. Colella, and F. B. Prinz, *Fuel Cell Fundamentals*, Wiley, New York (2009).
2. C. Hartnig, L. Jörissen, J. Kerres, W. Lehnert, and J. Scholta, in M. Gasik, ed., *Materials for fuel cells*, 101–184, Woodhead publishing, Cambridge (2008).
3. Y. Wang and K. S. Chen, in D. Stolten and B. Emonts, eds., *Fuel Cell Science and Engineering*, 839–878, WILEY-VCH, Weinheim (2012).
4. I. S. Hussaini and C. Y. Wang, *J. Power Sources*, **195**, 3830 (2010).
5. K. K. Poornesh, Y.-J. Sohn, G.-G. Park, and T.-H. Yan, *Int. J. Hydrogen Energy*, **37**, 15339 (2012).
6. N. Parikh, J. S. Allen, and R. S. Yassar, *Fuel Cells*, **12**, 382 (2012).
7. I. Manke, C. Hartnig, M. Grünerbel, W. Lehnert, N. Kardjilov, A. Haibel, A. Hilger, J. Banhart, and H. Rieseemeier, *Appl. Phys. Lett.*, **90**, 174105 (2007).
8. T. Sasabe, P. Deevanhxay, S. Tsushima, and S. Hirai, *J. Power Sources*, **196**, 8197 (2011).
9. U. Pasaogullari, C.-Y. Wang, and K. S. Chen, *J. Electrochem. Soc.*, **152**, A1574 (2005).
10. L. Hao and P. Cheng, *J. Power Sources*, **186**, 435 (2009).
11. A. C. Olesen, T. Berning, and S. K. Kær, *J. Fuel Cell Sci. Technol.*, **9**, 031010 (2012).
12. L. Chen, T.-F. Cao, Z.-H. Li, Y.-L. He, and W.-Q. Tao, *Int. J. Hydrogen Energy*, **37**, 9155 (2012).
13. P. Chippar and H. Ju, *Solid State Ionics*, **225**, 30 (2012).
14. X.-D. Niu, T. Munekata, S.-H. Hyodo, and K. Suga, *J. Power Sources*, **172**, 542 (2007).
15. H. Ostadi, P. Rama, Y. Liu, R. Chen, X. X. Zhang, and K. Jiang, *J. Membr. Sci.*, **351**, 69 (2010).
16. H. Ostadi, P. Rama, Y. Liu, R. Chen, X. Zhang, and K. Jiang, *Microelectron. Eng.*, **87**, 1640 (2010).
17. P. Rama, Y. Liu, H. Ostadi, K. Jiang, Y. Gao, X. Zhang, R. Fisher, and M. Jeschke, *Energy Fuels*, **24**, 3130 (2010).
18. P. Rama, Y. Liu, R. Chen, H. Ostadi, K. Jiang, X. Zhang, Y. Gao, P. Grassini, and D. Brivio, *Int. J. Numer. Methods Fluids*, **67**, 518 (2011).
19. Y. Gao, X. X. Zhang, P. Rama, Y. Liu, R. Chen, H. Ostadi, and K. Jiang, *Fuel Cells*, **12**, 365 (2012).
20. L. Chen, H.-B. Luan, Y.-L. He, and W.-Q. Tao, *Int. J. Therm. Sci.*, **51**, 132 (2012).
21. M. M. Daino and S. G. Kandlikar, *Int. J. Hydrogen Energy*, **37**, 5180 (2012).

22. P. P. Mukherjee, J. V. Coel, K. Jain, and A. Gidwani, *ECS Trans.*, **16**, 67 (2008).
23. L. Hao and P. Cheng, *J. Power Sources*, **186**, 104 (2009).
24. Y. Wang, S. Cho, R. Thiedmann, V. Schmidt, W. Lehnert, and X. Feng, *Int. J. Heat Mass Transfer*, **53**, 1128 (2010).
25. N. Zamel, X. Li, J. Becker, and A. Wiegmann, *Int. J. Hydrogen Energy*, **36**(9), 5466 (2011).
26. J. P. James, H.-W. Choi, and J. G. Pharoah, *Int. J. Hydrogen Energy*, **37**, 18216 (2012).
27. K. Schladitz, S. Peters, D. Reinelt-Blitzer, A. Wiegmann, and J. Ohser, *Comput. Mater. Sci.*, **38**, 56 (2006).
28. V. P. Schulz, J. Becker, A. Wiegmann, P. P. Mukherjee, and C.-Y. Wang, *J. Electrochem. Soc.*, **154**, B419 (2007).
29. R. Thiedmann, F. Fleischer, C. Hartnig, W. Lehnert, and V. Schmidt, *J. Electrochem. Soc.*, **155**(4), B391 (2008).
30. J. D. Hyman, P. K. Smolarkiewicz, and C. L. Winter, *Phys. Rev. E*, **86**, 056701 (2012).
31. D. Stoyan, W. S. Kendall, and J. Mecke, *Stochastic Geometry and its Applications*, J. Wiley & Sons, Chichester (1995).
32. R. Thiedmann, C. Hartnig, I. Manke, V. Schmidt, and W. Lehnert, *J. Electrochem. Soc.*, **156**(11), B1339 (2009).
33. A. Koponen, M. Kataja, and J. Timonen, *Phys. Rev. E*, **54**(1), 406 (1996).
34. A. Koponen, M. Kataja, and J. Timonen, *Phys. Rev. E*, **56**(3), 3319 (1997).
35. H. Okabe and M. J. Blunt, *Phys. Rev. E*, **70**, 066135 (2004).
36. D. Wolf-Gladrow, *Lattice-Gas Cellular Automata and Lattice Boltzmann Models*, Springer, Berlin (2000).
37. P. L. Bhatnagar, E. P. Gross, and M. Krook, *Phys. Rev.*, **94**(3), 511 (1954).
38. H. Herwig, *Strömungsmechanik A-Z*, Vieweg, Wiesbaden (2004).
39. J. T. Gostick, M. W. Fowler, M. A. Ioannidis, M. D. Pritzker, Y. M. Volkovich, and A. Sakars, *J. Power Sources*, **156**, 375 (2006).
40. J. T. Gostick, M. W. Fowler, M. D. Pritzker, M. A. Ioannidis, and L. M. Behra, *J. Power Sources*, **162**, 228 (2006).
41. A. Tamayol, F. McGregor, and M. Bahrami, *J. Power Sources*, **204**, 94 (2012).
42. L. M. Pant, S. K. Mitra, and M. Secanell, *J. Power Sources*, **206**, 153 (2012).
43. D. Froning, J. Brinkmann, U. Reimer, V. Schmidt, W. Lehnert, and D. Stolten, *Electrochim. Acta*, doi: 10.1016/j.electacta.2013.04.071 (2013).
44. J. Becker, R. Flückiger, M. Reum, F. N. Büchi, F. Marone, and M. Stampanoni, *J. Electrochem. Soc.*, **156**, B1175 (2009).
45. H. Wackernagel, *Multivariate Geostatistics: An Introduction with Applications*, Springer, Heidelberg (1997).
46. L. Sachs, *Angewandte Statistik*, Springer, Berlin, Heidelberg (2004).
47. J. Illian, A. Penttinen, H. Stoyan, and D. Stoyan, *Statistical Analysis and Modelling of Spatial Point Patterns*, J. Wiley & Sons, Chichester (2008).
48. O. Stenzel, D. Westhoff, I. Manke, M. Kasper, D. P. Kroese, and V. Schmidt, *Modell. Simul. Mater. Sci. Eng.*, **21**, 055004 (2013).
49. B. Baumeier, O. Stenzel, C. Poelking, D. Andrienko, and S. V., *Phys. Rev. B*, **86**, 184202 (2012).
50. O. Stenzel, L. J. A. Koster, R. Thiedmann, S. D. Oosterhout, R. A. J. Janssen, and V. Schmidt, *Adv. Funct. Mater.*, **22**, 1236 (2012).

## 6 Tables and Figures

Table 1: Notation of binder morphologies generated by different binder radius  $b_r$  and filling probability  $p$ , respectively

binder type	A	B	C	D	E
$b_r$ in $\mu\text{m}$	6	18	30	40	$\infty$
$p$	0.555	0.116	0.081	0.063	0.059

Table 2: Operating conditions of HT-PEFC

average current density	1 A/cm <sup>2</sup>
volumetric flow rate H <sub>2</sub>	7 ml/min
operating temperature	400 K
superficial velocity H <sub>2</sub>	1.7·10 <sup>-3</sup> m/s

Table 3: Measured permeabilities on Toray 090 reported by Hussaini et al.<sup>4</sup>

configuration	compression	permeability / $\mu\text{m}^2$	origin
through-plane	5 %	4.4	cited
	10 %	9	cited
	9 %	12.4 ± 0.88	measured
in-plane	0 %	20	cited
	9 %	14.6 ± 2	measured

Table 4: Simulated transport properties of binder models A, B, C, D, and E, averaged over 25 virtual geometries

orientation	A	B	C	D	E
permeability [ $\mu\text{m}$ ]	$16.52 \pm 1.21$	$15.91 \pm 1.34$	$15.27 \pm 1.46$	$13.71 \pm 1.58$	$13.04 \pm 1.79$
tortuosity	$1.34 \pm 0.02$	$1.38 \pm 0.03$	$1.39 \pm 0.03$	$1.47 \pm 0.04$	$1.50 \pm 0.07$

Table 5: Mean values and standard deviations of the coefficient of variation  $\rho_T$ , the global spatial variation  $g_T$ , and the range  $R$  in  $\mu\text{m}$  computed for the 25 fields of gas flow per binder type (bt)

bt	A	B	C	D	E
$\rho_T$	$1.20 \pm 0.09$	$1.24 \pm 0.09$	$1.24 \pm 0.10$	$1.33 \pm 0.12$	$1.44 \pm 0.20$
$g_T$ [ $\mu\text{m}$ ]	$29.23 \pm 3.61$	$31.50 \pm 4.14$	$33.97 \pm 5.6$	$40.15 \pm 9.79$	$46.03 \pm 10.46$
$R$ [ $\mu\text{m}$ ]	$34.74 \pm 3.26$	$36.78 \pm 4.62$	$38.94 \pm 4.83$	$42.30 \pm 6.48$	$46.08 \pm 7.57$

Table 6: Maximized correlation coefficient  $cor(\rho_T, \nu_i)$  and the corresponding number of layers  $i$  for the considered binder types

binder type	A	B	C	D	E
$\max_{i \in \{1, \dots, 26\}} cor(\rho_T, \nu_i)$	0.86	0.83	0.80	0.82	0.77
$\arg \max_{i \in \{1, \dots, 26\}} cor(\rho_T, \nu_i)$	2	3	3	4	5

Table 7: Fitted parameters for the stochastic model  $\Psi$  for gas flow fields

Binder type	A	B	C	E
$\lambda_S$ [ $\mu\text{m}^{-2}$ ]	0.00201	0.00161	0.00153	0.00146
$\lambda$ [ $\mu\text{m}^{-2}$ ]	0.00062	0.00061	0.00060	0.00056
$\lambda_P$ [ $\mu\text{m}^{-2}$ ]	$2.85 \cdot 10^{-6}$	$7.36 \cdot 10^{-6}$	$1.88 \cdot 10^{-5}$	$2.31 \cdot 10^{-5}$
$r_A$ [ $\mu\text{m}$ ]	90	67.5	52.5	60
$\nu_A$	0.07	0.1	0.15	0.23
$r_1$ [ $\mu\text{m}$ ]	12	11.85	9.9	8.7
$r_2$ [ $\mu\text{m}$ ]	45	47.25	56.25	56.5
$r_h$ [ $\mu\text{m}$ ]	3	3	3	3
$g_{min}$ [m/s]	-0.00014	-0.00025	-0.00017	-0.00018
$g_{max}$ [m/s]	0.02	0.022	0.023	0.031
$g_1$ [m/s]	1.32	1.15	1.12	0.75
$g_2$ [m/s]	0.00267	0.00292	0.003	0.00423
$\sigma$ [ $\mu\text{m}$ ]	15.0	15.75	15.75	16.5
$\kappa$ [ $\mu\text{m}$ ]	2.1	2.1	2.1	2.1

Table 8: Mean values (standard deviations) of the coefficients of variation  $\rho_T$  for the gas flow fields gained by LB simulations and drawn from the stochastic model  $\Psi$

binder type	A	B	C	E
$\rho_T$ via LB	1.20 (0.09)	1.24 (0.09)	1.24 (0.10)	1.44 (0.20)
$\rho_T$ via $\Psi$	1.21 (0.09)	1.24 (0.07)	1.25 (0.07)	1.43 (0.15)

Table 9: Fitted curves for all  $c_i$  accomplished by non-linear regression

	$\alpha_i$	$\beta_i$	$\gamma_i$
$c_1 (\lambda_S)$	0.00215	0.148	$4.5 \cdot 10^{-5}$
$c_2 (\nu_A)$	0.00026	-2.272	0.068
$c_3 (r_A)$	72.69	0.39	32.36
$c_4 (r_1)$	-0.00764	-2.175	12.18
$c_5 (r_2)$	0.47	-1.19	43.63
$c_6 (r_h)$	0	0	3
$c_7 (g_{min})$	$-9.14 \cdot 10^{-5}$	-0.146	$-4.01 \cdot 10^{-5}$
$c_8 (g_{max})$	$1.8 \cdot 10^{-6}$	-3.07	0.02
$c_9 (g_1)$	$-3.79 \cdot 10^{-4}$	-2.50	1.315
$c_{10} (g_2)$	$1.068 \cdot 10^{-8}$	-4.00	0.0027
$c_{11} (\sigma)$	0.049	-1.21	14.93
$c_{12} (\kappa)$	0	0	2.1

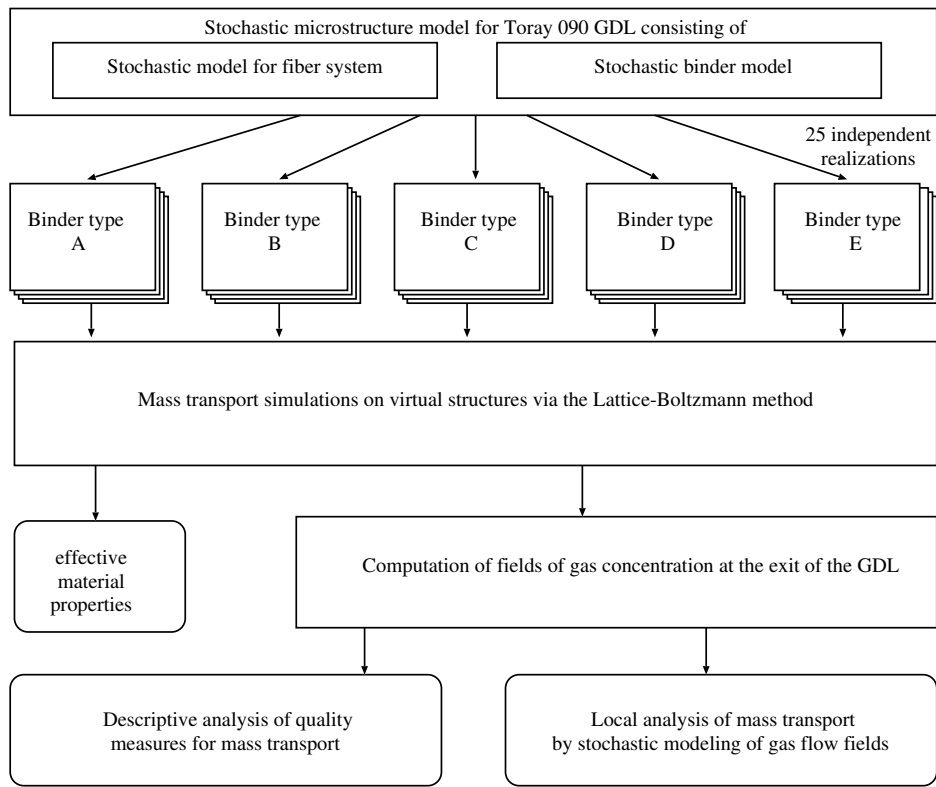


Figure 1: Flow-chart of the paper

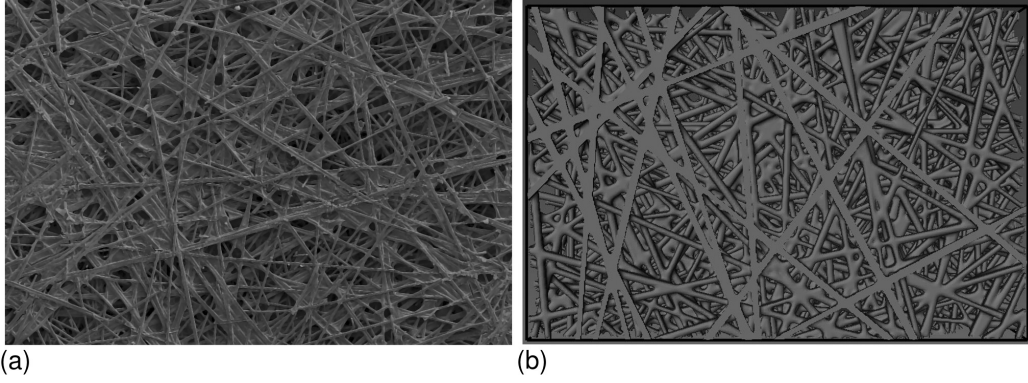


Figure 2: (a) 2D SEM image of Toray 090 GDL consisting of carbon fibers agglutinated by binder, (b) top-view on 3D paper-type GDL drawn from the stochastic model with binder radius  $b_r = 6 \mu\text{m}$  ( $p = 0.555$ )

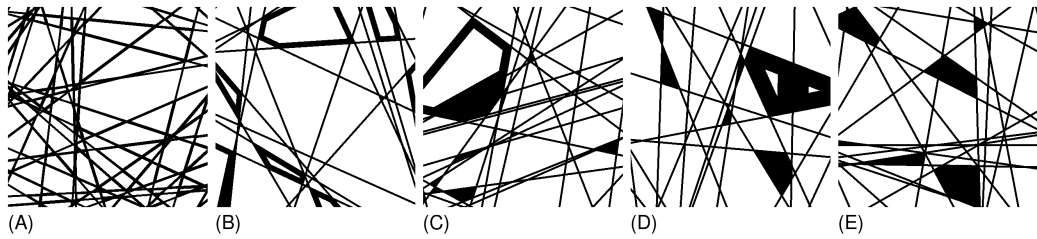


Figure 3: 2D slices of virtual paper-type GDL generated by the multi-layer model with different binder radii: (A)  $b_r = 6 \mu\text{m}$  ( $p = 0.555$ ), (B)  $b_r = 18 \mu\text{m}$  ( $p = 0.116$ ), (C)  $b_r = 30 \mu\text{m}$  ( $p = 0.081$ ), (D)  $b_r = 40 \mu\text{m}$  ( $p = 0.063$ ), and (E)  $b_r = \infty \mu\text{m}$  ( $p = 0.059$ )

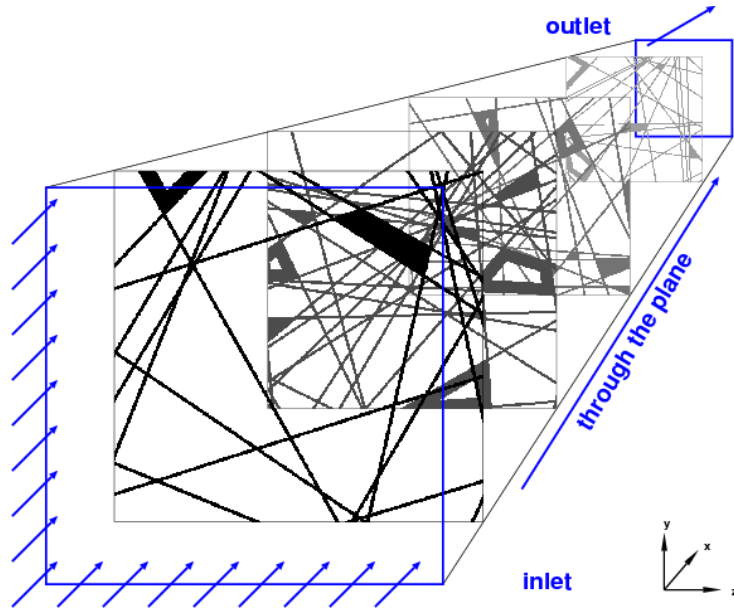


Figure 4: Simulation frame and coordinate axes of through-plane simulations

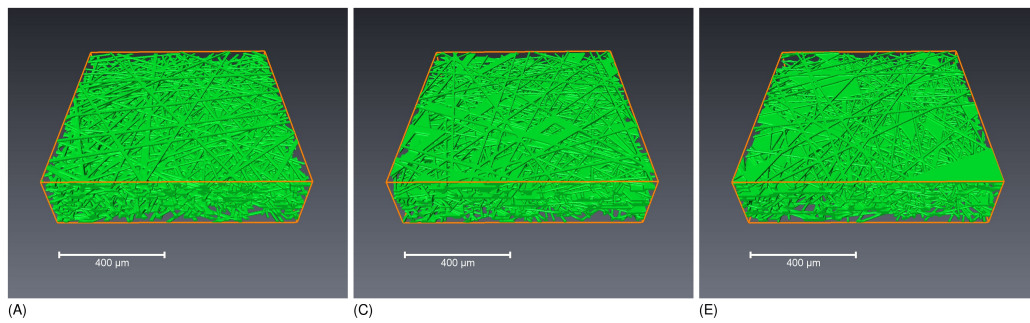


Figure 5: 3D paper-type GDL drawn from the stochastic microstructure model for binder type A ( $b_r = 6 \mu\text{m}$ ), binder type C ( $b_r = 30 \mu\text{m}$ ), and binder type E ( $b_r = \infty \mu\text{m}$ )

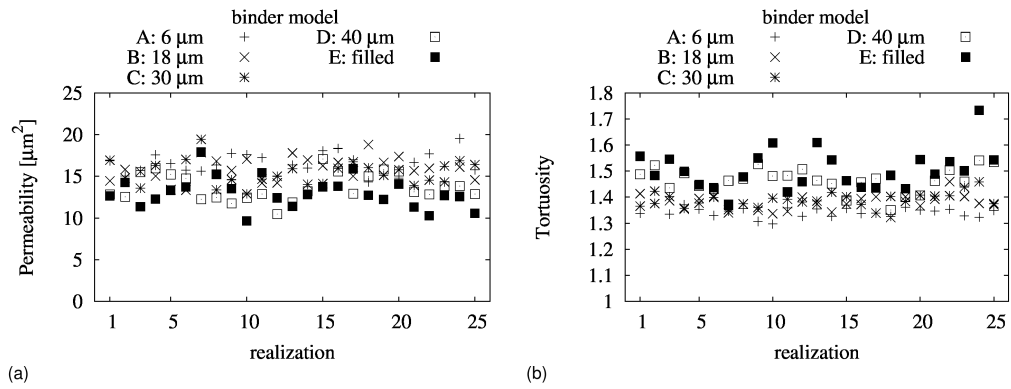


Figure 6: Statistical spread of effective transport properties from through-plane simulations on virtual microstructures

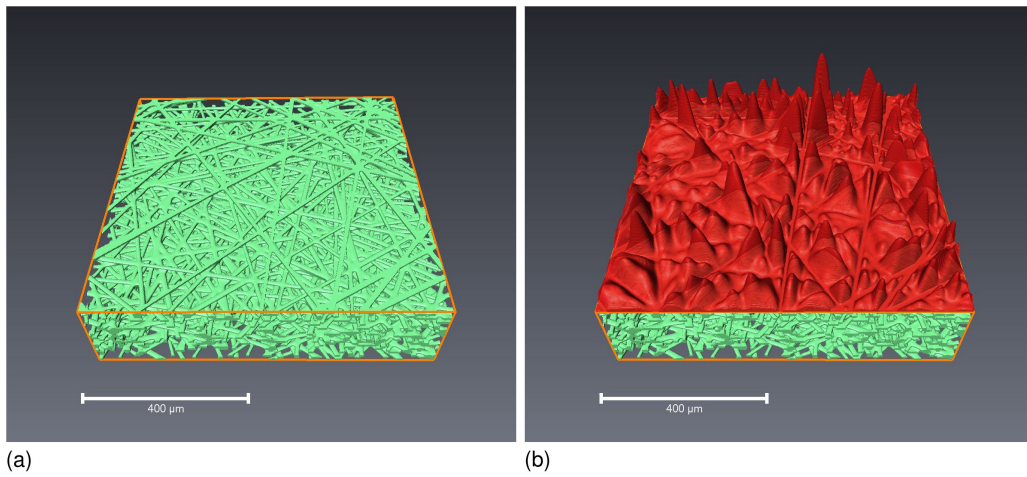


Figure 7: 3D paper-type GDL drawn from the stochastic microstructure model (a) and its gas flow field  $T$  (b)

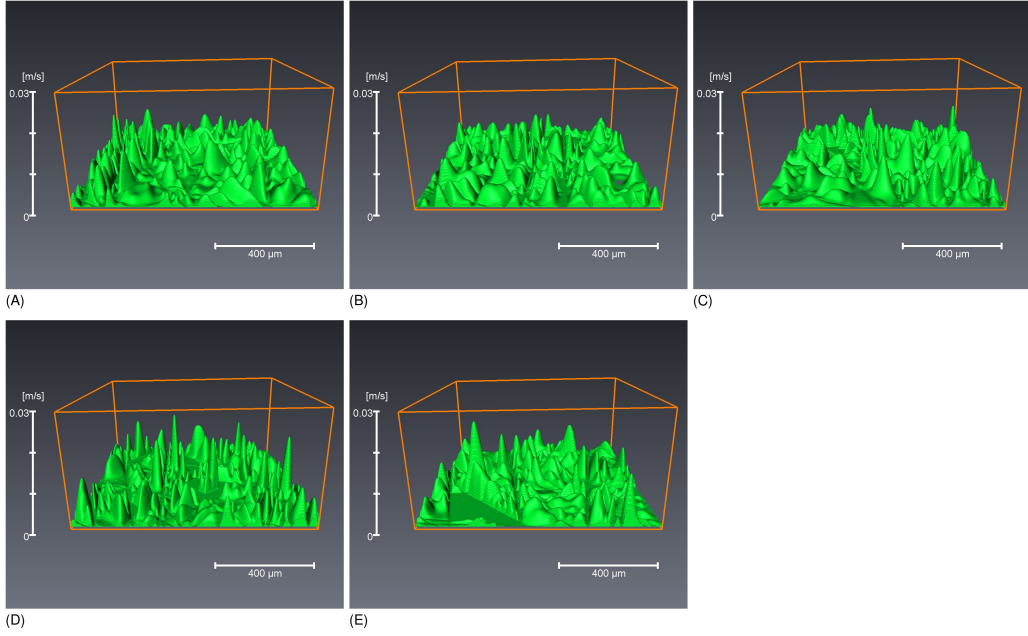


Figure 8: Gas flow fields  $T$  for binder type A ( $b_r = 6 \mu\text{m}$ ), B ( $b_r = 18 \mu\text{m}$ ), C ( $b_r = 30 \mu\text{m}$ ), D ( $b_r = 40 \mu\text{m}$ ), and E ( $b_r = \infty \mu\text{m}$ )

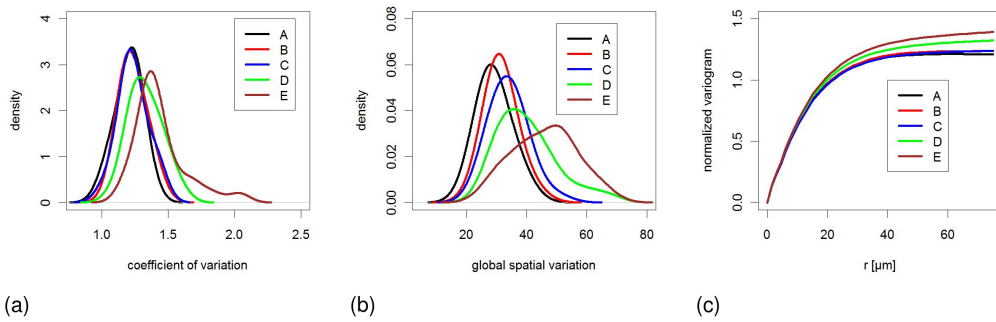


Figure 9: Histograms of the coefficient of variation  $\rho_T$  (a), the global spatial variation  $g_T$  (b), and point-wise averaged normalized variograms (c) computed for the 25 fields of gas flow per binder type

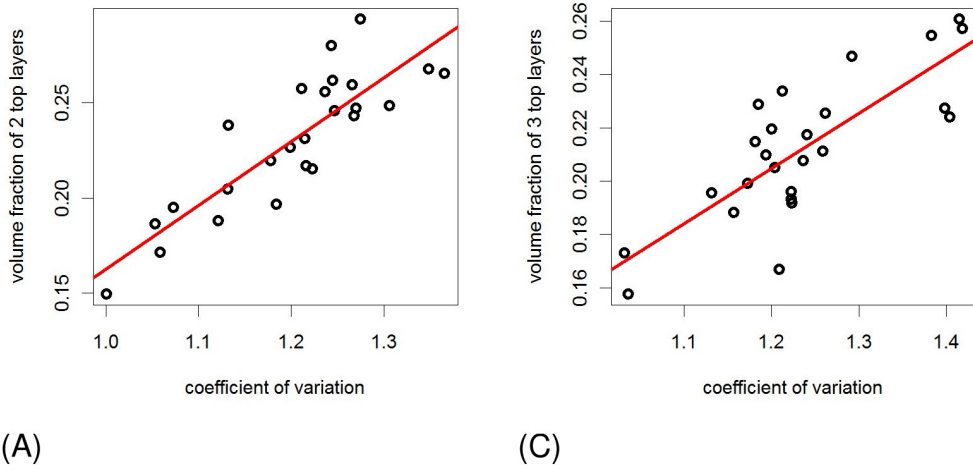


Figure 10: Scatter plot of  $\nu_{\arg \max_{i \in \{1, \dots, 26\}} \text{cor}(\rho_T, \nu_i)}$  and  $\rho_T$  for binder types A and C. Number of top layers according to Table 6.

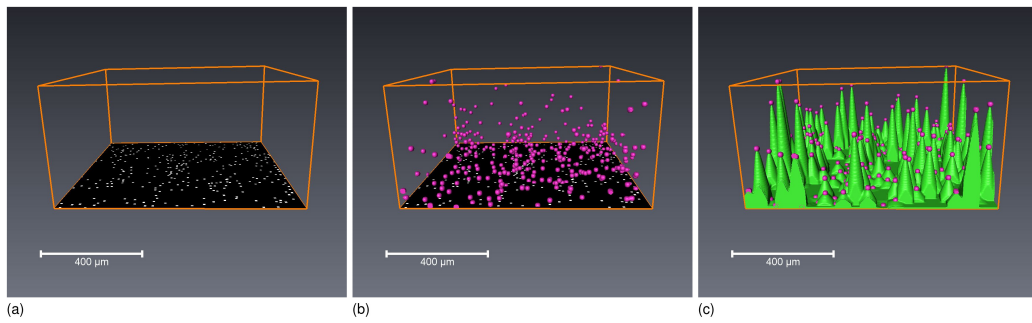


Figure 11: Basic modeling idea for fields of gas flow: choose a 2D point process representing the locations of the bells (a), add height information to the point process (b), and take the union of truncated Gaussian bells (c)

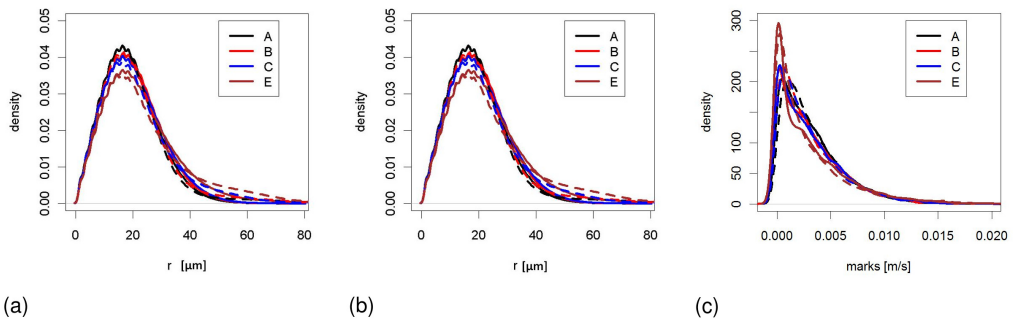


Figure 12: Pointwise averaged pair-correlation functions (a), histograms of spherical contact distances (b), and histograms of marks (c) computed for the extracted (solid lines) and simulated (dashed lines) point patterns of local extrema for each binder type A, B, C, E

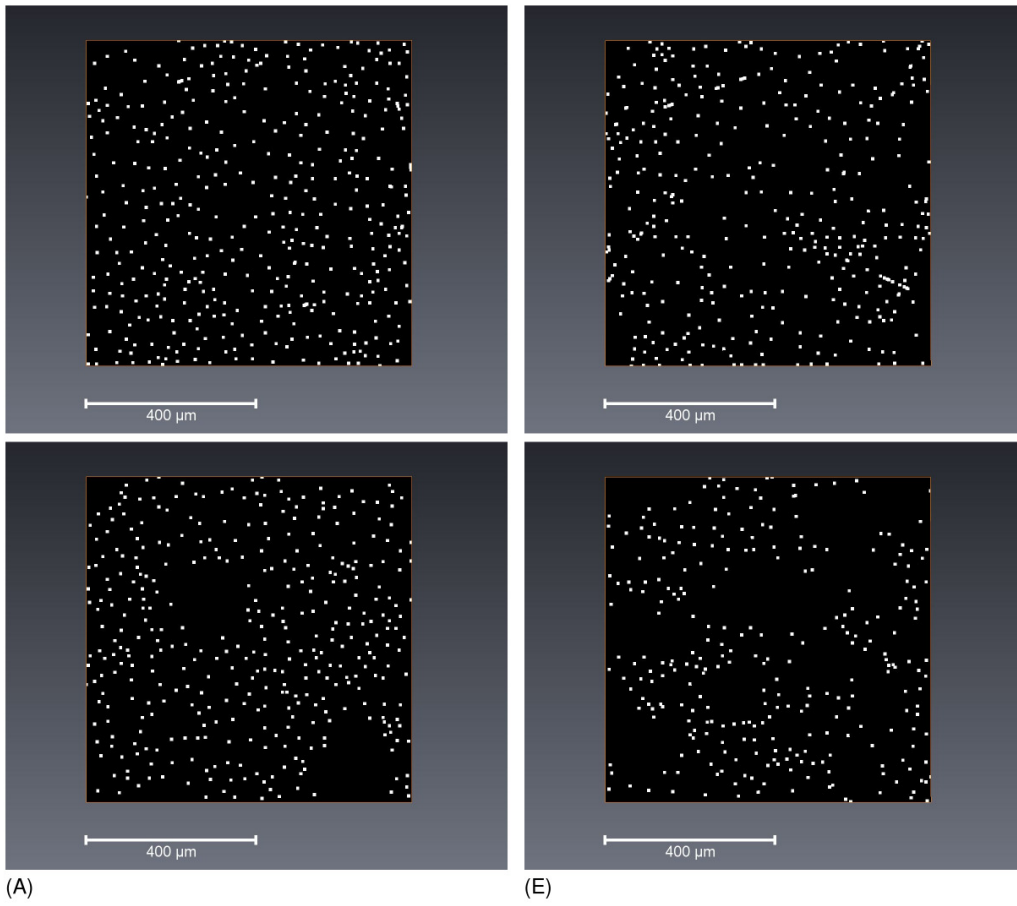


Figure 13: Local maxima of gas flow fields (top) and simulated point patterns drawn from the fitted point-process models (bottom) for the binder type A and E

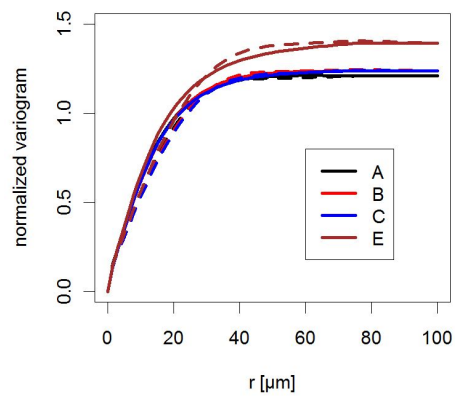


Figure 14: Pointwise averaged normalized variograms for the gas flow fields computed via the LB method (solid lines) and computed for simulations drawn from the stochastic model  $\Psi$  (dashed lines)

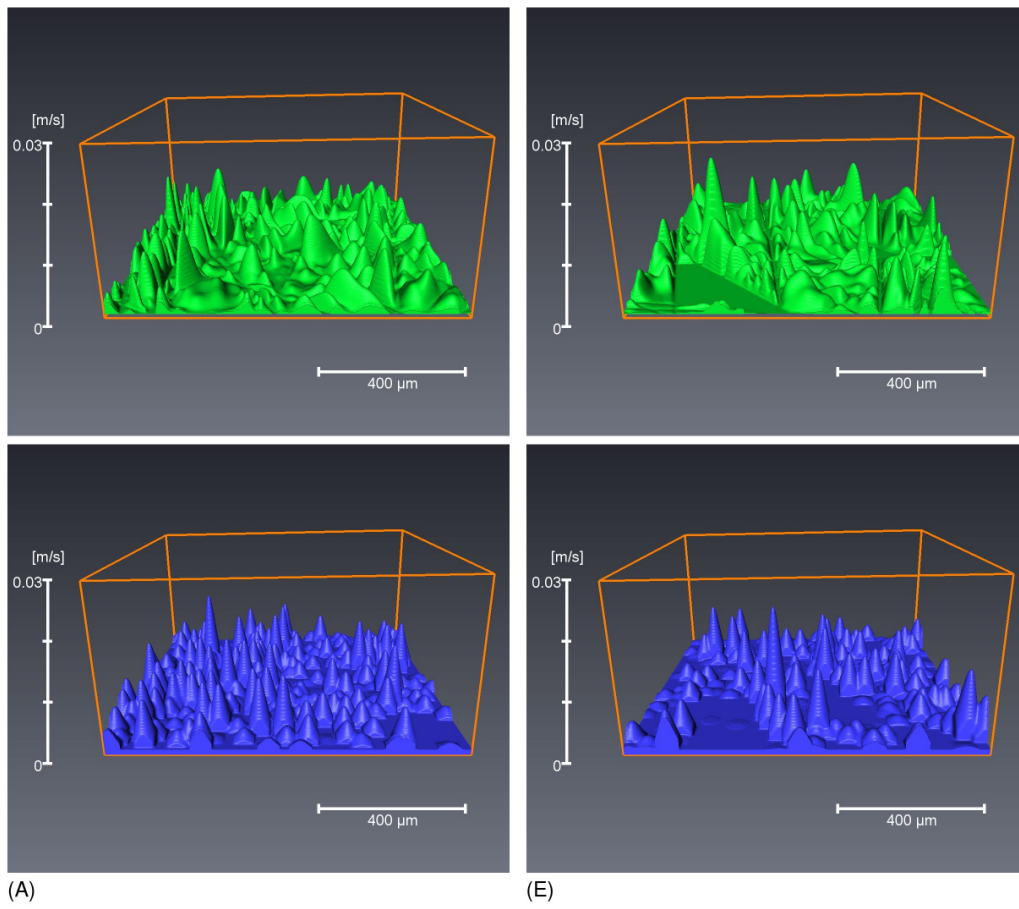


Figure 15: Gas flow fields computed via the LB method (top) and simulated fields drawn from the stochastic model  $\Psi$  (bottom) for binder types A and E

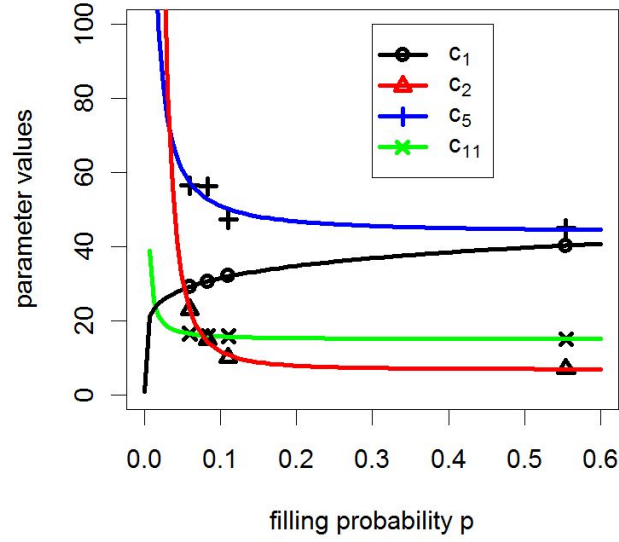


Figure 16: Non-linear regression curves for the parameters  $\lambda_S \cdot 20000$  (i.e.,  $c_1 \cdot 20000$ ),  $\nu_A \cdot 100$  (i.e.,  $c_2 \cdot 100$ ),  $r_2$  (i.e.,  $c_5$ ), and  $\sigma$  (i.e.,  $c_{11}$ )

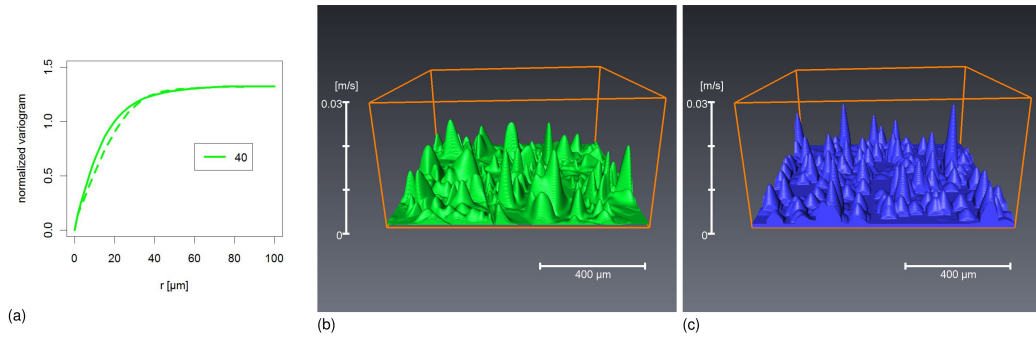


Figure 17: (a) pointwise averaged normalized variograms for the gas flow fields computed via LB method (solid lines) and computed for simulations drawn from the stochastic model  $\Psi$  (dashed lines), (b) gas flow field gained by LB simulations for binder type D, (c) gas flow field drawn from the predictive stochastic model  $\Psi_{(c_1(0.063), \dots, c_{12}(0.063))}$  for binder type D